Journal of Power Sources 195 (2010) 1895–1904

Contents lists available at ScienceDirect

Journal of Power Sources

journal homepage: www.elsevier.com/locate/jpowsour

Thermal stress and thermo-electrochemical analysis of a planar anode-supported solid oxide fuel cell: Effects of anode porosity

Lieh-Kwang Chiang*, Hui-Chung Liu, Yao-Hua Shiu, Chien-Hsiung Lee, Ruey-Yi Lee

Institute of Nuclear Energy Research, Taoyuan County 32546, Taiwan, ROC

ARTICLE INFO

Article history:
Received 20 August 2009
Received in revised form 6 October 2009
Accepted 6 October 2009
Available online 13 October 2009

Keywords:
Solid oxide fuel cell
Computational fluid dynamics
Thermal stress analysis

ABSTRACT

A 3D integrated numerical model is constructed to evaluate the thermal-fluid behavior and thermal stress characteristics of a planar anode-supported solid oxide fuel cell (SOFC). Effects of anode porosity on performance, temperature gradient and thermal stress are investigated. Using commercial Star-CD software with the es-sofc module, simulations are performed to obtain the current–voltage (*I–V*) characteristics of a fuel cell as a function of the anode porosity and the temperature distribution within the fuel cell under various operating conditions. The temperature field is then imported into the MARC finite element analysis (FEA) program to analyze thermal stresses induced within the cell. The numerical results are found to be in good agreement with the experimental data. It is shown that the maximum principal stress within the positive electrode–electrolyte–negative electrode (PEN) increases at a higher current and a higher temperature gradient. It is recommended that the temperature gradient should be limited to less than 10.6 °C mm^{-1} to maintain the structural integrity of the PEN.

1. Introduction

With growing international concern regarding the depletion of the world's natural resources and the need for greater environmental protection, the problem of developing renewable energy sources has attracted significant attention in recent years. Solid oxide fuel cells (SOFCs), in which energy is produced via an electrochemical conversion process, have a high efficiency, good fuel flexibility, low emissions, and good long-term stability. As a result, they are widely regarded as an ideal solution for meeting the future energy needs of both industrial and private consumers. However, SOFCs require a high operating temperature in order to induce an internal reforming reaction within the anode. Consequently, various temperature-related problems exist in ensuring their long-term mechanical integrity, including high degradation rates, high-temperature gradients, significant thermo-stresses, and so.

As a result, the literature contains many experimental and theoretical investigations into various aspects of typical SOFCs. For example, in [1–4], X-ray reflection and ring-on-ring methods were used to measure the residual stress and flexural strength of the PEN within an SOFC at room or elevated temperatures. Many researchers have utilized experimental techniques to examine the effects of the operating parameters on the behavior and performance of typical SOFCs [5–9]. Other researchers have used numerical methods to examine the thermal-fluid behavior and thermal stress characteristics of different SOFC structures, including single units [10–12], single cells [13–15], and single/multi-cell stacks [16–18]. For example, Yakabe et al. [10–12] used Star-CD, a commercial computational fluid dynamics (CFD) tool, to calculate the fuel concentration, temperature and current density distribution in a planar SOFC. The temperature field within the SOFC was then input to a finite element analysis (FEA) program (ABAQUS) to evaluate the thermal stress induced with the SOFC structure. The results showed that a co-flow pattern was advantageous in reducing the temperature difference between the various components in the SOFC structure, thereby minimizing the internal stresses within the device. Liu et al. [14,15] performed CFD simulations to calculate the reaction rate, fuel concentration, gas flow rate, temperature distribution, and current density in a single cell tested under various operating conditions. The resulting thermally induced stresses were then analyzed using commercial FEA software (MARC). Khaleel et al. [17,18] integrated commercial MARC FEA code with an in-house electrochemical module to accomplish the modeling and characterization of planar-type SOFCs. Selimovic et al. [19] utilized an in-house tool to evaluate the electrochemical and thermal performance of a bipolar planar cell and substituted the temperature field data into the commercial FEMLAB program to calculate the corresponding distribution of the thermal stress. Weil and Koppel [20,21] utilized

* Corresponding author at: Institute of Nuclear Energy Research, No. 1000, Wunhua Rd., Jiaan Village, Longtan Township, Taoyuan County 32546, Taiwan (R.O.C.). Tel.: +886 23 4711400; fax: +886 23 4711409.
E-mail address: kwang@iner.gov.tw (L.-K. Chiang).

0378-7753/$ – see front matter © 2009 Elsevier B.V. All rights reserved.
doi:10.1016/j.jpowsour.2009.10.011

Nomenclature

A_i	pre-exponential factor, A m^{-2}
c_p	constant-pressure specific heat, J(kg K)$^{-1}$
$\bar{c}$	mean constant-volume specific heat, J(kg K)$^{-1}$
d	thickness, m
D	mass diffusivity, m^2 s^{-1}
$[D]$	elasticity matrix
E	Young's modulus, GPa
E_{act}	activation energy, J mol^{-1}
F	Faraday constant, 96,487 C mol^{-1}
F_h	diffusional energy flux
F_m	diffusional flux
h	static enthalpy, J kg^{-1}
H	heat of formation, J kg^{-1}
i	current density, A m^{-2}
i_0	exchange current density, A m^{-2}
k	electrochemical reaction rate constant
$[k]$	stiffness matrix
M	molecular weight, g
$\bar{m}^0$	initial weight fraction
P	pressure, Pa
p	porosity after reduction
R	universal gas constant, 8.314 J(mol K)$^{-1}$
R_i	resistance, Ω
R_m	rate of mass production or consumption
T	temperature, K
u_i	local velocity, m s^{-1}
V	operating voltage, V
$\dot{V}$	gas flow rate, ml min^{-1}
Y	mass fraction
Y_m	mass fraction of the different species components with molecular weight

Greek symbols

ρ	density, kg m^{-3}
τ	stress tensor
$[\sigma]$	stress vector
$[\varepsilon]$	strain vector
ε	porosity
δ	point deflection

Subscripts

a	anode
c	cathode
H_2	hydrogen
O_2	oxygen
eff	effective
f	failed strength
m	mth composition of fuel reactant

commercial ANSYS software to analyze the thermal strain and stress in the bonded compliant seal (BCS) used to seal the cell and window frame components in planar SOFCs. The results confirmed the effectiveness of the BCS design in decoupling the effects of differential thermal expansion between the two components, but showed that some bowing took place within the cell.

This study constructs a 3D numerical model of an anode-supported planar SOFC and then performs a series of simulations using Star-CD code and the es-sofc module to investigate the current–voltage (I–V) characteristics of the fuel cell and to determine the temperature field over a range of anode porosities and operating conditions. The temperature data are then imported into the MARC FEA program to compute the corresponding thermal stress distribution. Fig. 1 presents a flow chart of the overall simulation procedure. The validity of the numerical model is confirmed by comparing the simulated I–V characteristics of the SOFC with the experimental observations. Having confirmed the validity of the model, simulations are performed to investigate the maximum principal stress induced within the PEN as a function of the operating voltage, temperature gradient and anode porosity.

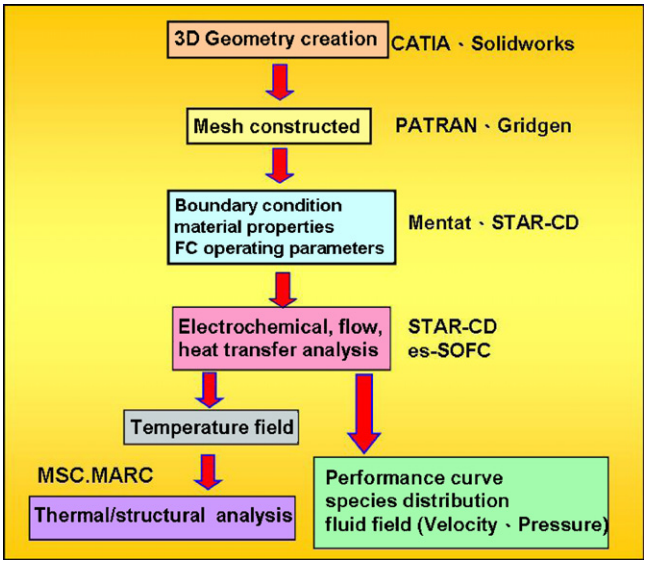

Fig. 1. Flow chart showing overall simulation procedure for thermo-electrochemical/thermal stress analysis of single SOFC cell.

2. Experimental

2.1. Single-cell performance tests

To validate the performance of the numerical model, a series of experiments was performed using the single-cell planar SOFC test station constructed at the Institute of Nuclear Energy Research (INER) in Taiwan (see Fig. 2(a)). During the experiments, hydrogen gas was supplied to the anode compartment of the fuel cell, while air was supplied to the cathode compartment. A cell with dimensions of 10 cm × 10 cm was sandwiched between two alumina gas distributors with Pt current collecting meshes. As shown in Fig. 2(a), the cell incorporated Pt and Ni meshes on the cathode and anode sides, respectively, to act as electrical collectors for the voltage and current probes used to analyze the I–V characteristics of the fuel cell.

The oxidant and fuel gases were flowed separately to the center of the upper and lower surfaces of the PEN via circular inlet pipes and were then distributed over the PEN surface. The effective area of the PEN was around 81 cm^2. The NiO/YSZ anode was gradually reduced via an oxidation process during the warming-up process performed at a heating rate of 1 °C min^{-1} with a fuel gas composition of 10%H_2/90%N_2. When the temperature of the PEN reached the preset point of 775 °C, the H_2 concentration was gradually increased to 100% hydrogen and humidified at room temperature by bubbling method in steps of 10% every 10 min. Once the electrochemical response of the cell converged to steady-state conditions (as indicated by a PEN temperature of 800 °C and a H_2 concentration of 100%), the I–V characteristics of the cell were measured using the current and voltage probes attached to the Pt and Ni meshes on the cathode and anode sides of the SOFC, respectively.

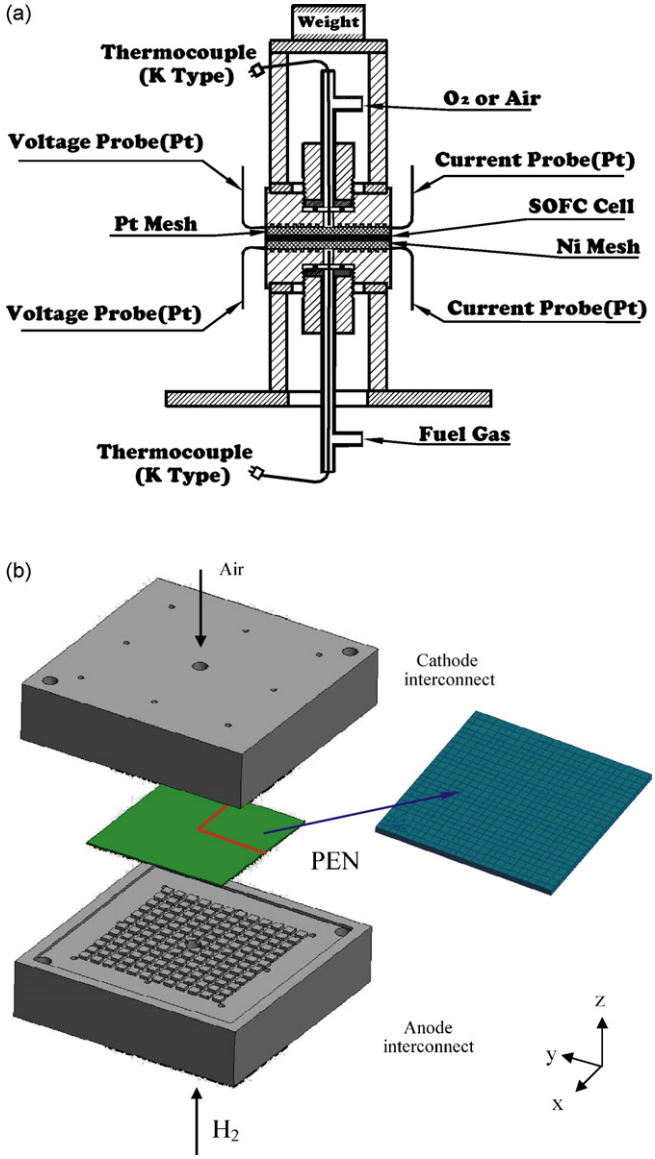

Fig. 2. (a) Schematic illustration of cell test station and (b) schematic illustration of 3D test cell model.

2.2. Flexural strength measurement

The high-temperature mechanical properties of the various components within the SOFC play an essential role in determining its mechanical integrity under normal operating conditions. Of all the components within the SOFC, the PEN is particularly liable to embrittlement under high temperatures. As a consequence, determining the flexural strength of the PEN over a wide range of operating conditions is essential in ensuring the reliability and performance of the device. In this study, the flexural strength of various reduced and unreduced ASC (anode-supported cell) specimens was measured by performing ring-on-ring biaxial strength tests in accordance with the test procedure laid down in ASTM C-1499. According to ASTM C-1499, the equi-biaxial strength, σ_f, of a specimen is given by

$$\sigma_f = \frac{3F_L}{2\pi h^2}\left[(1-\nu)\frac{D_S^2 - D_L^2}{2D^2} + (1+\nu)\ln\frac{D_S}{D_L}\right], \quad (1)$$

where h is the thickness of the specimen, F_L is the applied force, and D, D_S and D_L are the diameters of the specimen, support ring and load ring, respectively. In general, the Young's modulus of a circular specimen can be obtained from ASTM C-1499

$$E = \frac{3F(1-\nu^2)D_L^2}{8\pi\delta_0 h^3}\left(\frac{D_S^2}{D_L^2}\left[1 + \frac{(1-\nu)(D_S^2 - D_L^2)}{2(1+\nu)D^2}\right] - \left(1 + \ln\frac{D_S}{D_L}\right)\right), \quad (2)$$

where δ_0 is the deflection of the center point of the specimen. However, in the ring-on-ring tests performed in this study, the deflection is measured at the point where the load ring contacts the specimen rather than at the center point. As a result, Eq. (2) is modified to the form [27]

$$E = \frac{3F(1-\nu^2)D_L^2}{8\pi\delta_L h^3}\left(\frac{D_S^2}{D_L^2} + \left[\frac{(1-\nu)(D_S^2 - D_L^2)(D_S^2 - D_L^2)}{2(1+\nu)D^2 D_L^2}\right] - \left(1 + 2\ln\frac{D_S}{D_L}\right)\right), \quad (3)$$

where δ_L is the deflection at the point of contact between the specimen and the load ring.

Table 1
Input parameters for SOFC simulations.

PEN thickness	600 μm
Anode thickness	560 μm
Electrolyte thickness	5 μm
Cathode thickness	35 μm
Rib thickness	1 mm
Gas distributors thickness	30 mm
Operating temperature	800 °C
Operating pressure	1 atm
Cell temperature	800 °C
Anode fuel	H_2
Cathode fuel	Air
Fuel inlet temperature (anode and cathode)	760 °C
Pre-exponential factor, A_i	128
Activation energy, E_{act}	550 J mol^{-1}

3. Numerical method

3.1. Geometric model

In this study, the thermal-fluid behavior and electrochemical reactions within the SOFC cell were analyzed numerically using a 3D model. The temperature field computed in the simulations was then imported to the MARC FEA program in order to calculate the thermal stress within the PEN. Fig. 2(b) illustrates the basic components within the numerical model, namely a PEN electrode and two alumina gas distributors (one on either side of the PEN). The gas flow configuration consists of multiple ribs measuring 3 mm × 3 mm × 1 mm on the alumina gas distributors and a circular gas inlet channel in the center of both gas distributors. The major parameters of the numerical model are summarized in Table 1.

3.2. Thermal-fluid model

In the present simulations, the Navier–Stokes equation is solved for each of the computational mesh elements within the fluid region. To simplify the calculations, the following assumptions are made: (1) the fuel and oxidant gases are ideal gases; (2) the gas flow is steady and laminar everywhere in the cell channels; and (3) the anode and cathode materials are isotropic porous media. Given these assumptions, the governing equations for the conservation of mass, momentum, enthalpy and species are formulated as follows [14]:

Mass equation

$$\frac{\partial \varepsilon \rho u_i}{\partial x_i} = 0. \quad (4)$$

where ε is the porosity of porous media (equals to zero in the flow channel region) and u_i is the local velocity of fuel defined by Darcy law [28]:

$$u_i = -\frac{k}{\varepsilon\mu}\nabla P \tag{5a}$$

Momentum equation

$$\frac{\partial}{\partial x_j}(\varepsilon\rho u_j u_i - \tau_{ij}) = -\varepsilon\frac{\partial P}{\partial x_i} + \frac{\varepsilon^2\mu u_i}{k}, \tag{5b}$$

where τ_{ij} is the stress tensor relative to the velocity gradient and $\varepsilon^2\mu u_i/k$ is equal to zero in the flow channel region. In addition, the density of the fuel mixture is given by the ideal gas law as

$$\rho = \frac{P}{RT(\sum_m (Y_m/M_m))} \tag{6}$$

where Y_m is the mass fraction of the different species components with molecular weight M_m.

Enthalpy equation

$$\frac{\partial}{\partial x_j}(\rho h u_j + F_{h,j}) = \frac{\partial P}{\partial t} + u_j\frac{\partial P}{\partial x_j} + \tau_{ij}\frac{\partial u_i}{\partial x_j} + s_h. \tag{7}$$

In the above equations, source terms s_h represent the heat generation from chemical reaction and the specific enthalpy h of the fluid is defined as the sum of the thermal and chemical components, i.e.

$$h = c_p T - c_p^0 T^0 + \Sigma Y_m H_m, \tag{8}$$

where H_m is the heat of formation of constituent m and c_p is the mean constant-pressure specific heat at temperature T with c_p^0 being the reference specific heat at a reference temperature T^0. For solids and constant-density fluids, the transport equation for a specific internal energy e is given by

$$e = \bar{c}T - \bar{c}^0 T^0 + \Sigma Y_m H_m, \tag{9}$$

where $\bar{c}$ is the constant-volume specific heat.

Species equation

$$\frac{\partial}{\partial x_j}(\rho u_j Y_m + F_{m,j}) = R_m, \tag{10}$$

where F_m is the diffusion flux component and R_m is the rate of mass production or consumption during the chemical reaction.

3.3. Electrochemical model

The numerical solution procedure includes various electrochemical reaction and net enthalpy generation calculations, including the combustion of oxygen with hydrogen and the gas–water-shift reaction. In the computation process, the amount of oxygen at the cathode side which subsequently reacts with the hydrogen at the anode side in accordance with $H_2 + (1/2)O_2 \rightarrow H_2O$ is determined by the specified current density.

The limiting current densities for the chemical reactions in the anode and cathode, respectively, are specified as [6]

$$i_a = \frac{2FD_{eff}(T)P_{H_2}}{RTd_a}, \tag{11}$$

$$i_c = \frac{4FPD_{eff}(T)}{RTd_c}\ln\left(\frac{P_{system}}{P_{system} - P_{O_2}}\right), \tag{12}$$

where $D_{eff}(T)$ is the effective diffusion coefficient and is given by

$$D_{eff}(T) = D(T)\cdot\varepsilon^{1.5}, \tag{13}$$

while P_{H_2} and P_{O_2} are the partial pressures of hydrogen and oxygen, respectively, F is the Faraday constant, and d_a and d_c are the thicknesses of the anode and cathode electrodes, respectively.

The electrical performance of the SOFC is evaluated from the fuel and air compositions. The cell voltage is calculated as

$$V(i) = V_{Nernst} - V_{Ohmic} - V_{Butler-Volmer} + V_{cathode} + V_{anode}, \tag{14}$$

where V_{Nernst} is the Nernst or open circuit potential, V_{ohmic} is the ohmic potential drop, and $V_{Butler-Volmer}$, V_{anode} and $V_{cathode}$ are the Butler–Volmer, anode and cathode polarizations, respectively. The various voltage terms in Eq. (14) are defined as follows:

$$V_{Nernst} = \frac{RT}{4F}\ln\left(\frac{P_{O_2,anode}}{P_{O_2,cathode}}\right), \tag{15}$$

$$V_{Ohmic} = iR_i, \tag{16}$$

$$V_{Butler-Volmer} = \frac{RT}{\alpha F}\sinh^{-1}\left(\frac{i}{2i_0}\right), \tag{17}$$

$$V_{cathode} = \frac{RT}{4F}\ln\left(1 - \frac{i}{i_c}\right), \tag{18}$$

$$V_{anode} = \frac{RT}{2F}\ln\left(1 - \frac{i}{i_a}\right). \tag{19}$$

Note that in Eq. (17), the exchange current density i_0 corresponds to the dynamic electron transfer rate under equilibrium conditions and is expressed in accordance with [17] as

$$i_0 = A_i\cdot\exp\frac{-E_{act}}{RT}, \tag{20}$$

where the pre-factor A_i and activation energy E_{act} are properties specific to the electrode–electrolyte interface in the electrochemical model. In the present study, the pre-factor A_i is estimated from the experimental I–V curves.

Boundary conditions for the dependent variables of the transport equations at the interfaces between different layers of the same domain are not required. However, fully developed flow conditions are assumed at the fuel and air flow outlets, i.e.

$$\frac{\partial u_i}{\partial z} = \frac{\partial Y_m}{\partial z} = 0. \tag{21}$$

Meanwhile, the boundary conditions at the interfaces between the flow field and the gas distributors are specified as

$$u_i = Y_m = 0. \tag{22}$$

Similarly, the boundary conditions at the interfaces between the flow field and the PEN are given as

$$\varepsilon_{eff}\left.\frac{\partial u_i}{\partial z}\right|_{z=z_{MEA}} = \left.\frac{\partial u_i}{\partial z}\right|_{z=z_{flowfield}}, \qquad \varepsilon_{eff}u_i| = u_i| \tag{23a}$$

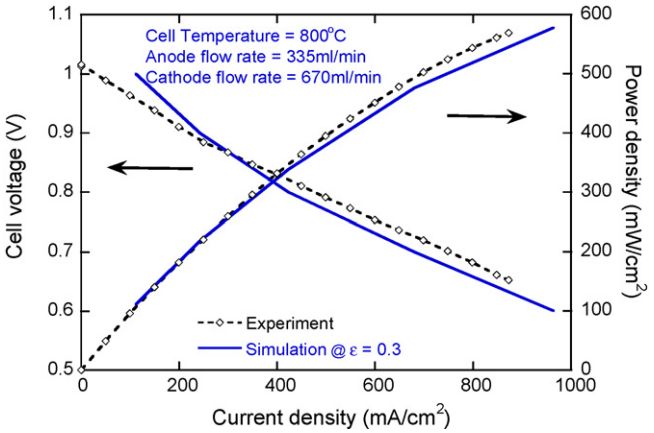

Fig. 3. Comparison of experimental and numerical results for variation of cell voltage and power density with current density.

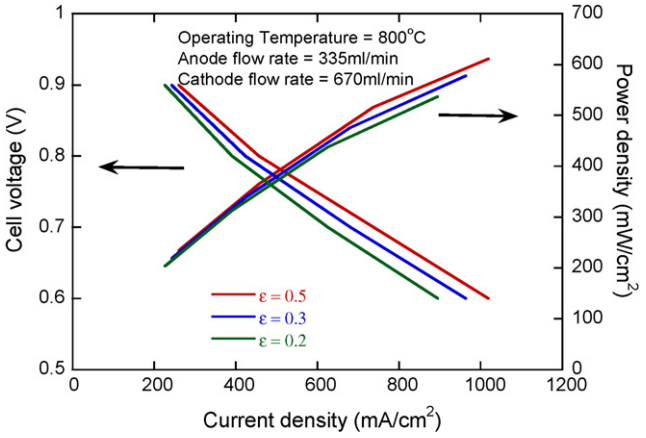

Fig. 4. Variation of cell voltage and power density with current density as function of anode porosity.

$$\varepsilon_{eff}\left.\frac{\partial Y_m}{\partial z}\right|_{z=z_{MEA}} = \left.\frac{\partial Y_m}{\partial z}\right|_{z=z_{flowfield}}, \qquad Y_m\,| = Y_m\,| \tag{23b}$$

Finally, the boundary conditions at the interface between the electrolyte and the electrodes are specified as

$$\left.\frac{\partial u_i}{\partial z}\right|_{z=z_{electrolyte}} = 0, \qquad \left.\frac{\partial Y_m}{\partial z}\right|_{z=z_{electrolyte}} = 0. \tag{24}$$

Since the test cell has a symmetric geometry, the 3D FEA model constructed in this study considered just one quarter of the test cell configuration. The model was constructed using PATRAN software (MSC Inc.), and comprised a total of 17,974 sold elements (Type 84) and 24,218 nodes. Having constructed the model, the CFD computational domain was meshed using GRIDGEN. Each element within the mesh was then taken as a control volume in the Star-CD finite-volume solution procedure. In other words, the governing equations were numerically integrated over each control volume, where all of the related variables and material properties were stored at the cell center.

3.4. Thermal stress model

The temperature profiles generated by the Star-CD and es-sofc simulations were imported into the MARC FEA program to calculate the thermal stress distributions within the SOFC test cell. In transferring the temperature profiles to MARC, the temperature data were read into the nodes and were then interpolated to the corresponding points within each element. Since the format of the temperature data generated in the Star-CD simulations was not directly compatible with the data requirements of MARC, a proprietary subroutine was programmed in FORTRAN 77 to resolve the incompatibility issue. In performing the MARC analyses, a "touch-bonding constraint" condition was specified between the PEN and its adjacent components. In addition, a frictional coefficient of 0.16 was specified for the contact conditions between all neighboring components in the cell [22]. Moreover, an assumption was made that the SOFC cell was simply supported on its lower surface. As a result, the entire surface of the lower interconnect of the cell was constrained in the direction normal to the lower plane. In addition, a uniform load was imposed on the surface of the upper interconnect such that a close contact was maintained between the PEN and the upper and lower (cathode and anode) gas distributors. Finally, an additional constraint was applied to the edge points on the symmetric plane to prevent rigid body motion of the entire test cell.

In a previous study by the current group [15], the temperature-dependent elastic properties of a NiO-YSZ anode [23] were evaluated without considering the anode porosity. However, in practice, the mechanical properties of Ni-based anode materials depend strongly on their porosity [24]. Thus, in this study, the elastic modulus, Poisson's ratio and biaxial strength of the Ni-YSZ anode (in both an unreduced and a reduced condition) were modeled as a function of the anode porosity. Radovic [24] and Selcuk [25,26] presented the effective mechanical properties of various materials of interest for SOFC applications (e.g. YSZ, GCO, TZP, NiO-YSZ) based upon a theoretical treatment of the porosity effect (i.e. the composite sphere method, CSM) and an empirical treatment (i.e. exponential, nonlinear, and linear equations), respectively. For NiO-YSZ, the empirical equations were shown to provide better results than the CSM equations [25]. Thus, in the present simulations, the Young's modulus, Poisson's ratio and biaxial strength of the NiO-YSZ and Ni-YSZ anodes are calculated at different porosities on the basis of empirical equations. In evaluating the effect of the reduction process on the porosity of the anode, the porosity after reduction, p, was derived directly from the initial (unreduced) porosity, p_0, in accordance with [24]

$$p = p_0 + (1 - p_0)\cdot \tilde{m}^0_{NiO}\cdot\left[\frac{1}{\rho_{NiO}} - \frac{1}{\rho_{Ni}} + \frac{m_0}{m_{NiO}}\cdot\frac{1}{\rho_{Ni}}\right], \tag{25}$$

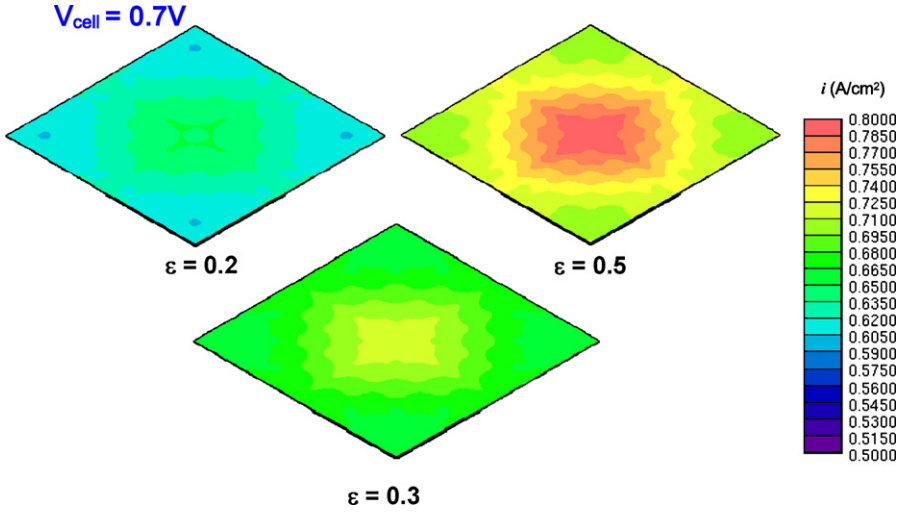

Fig. 5. Effects of anode porosity on current density distribution in PEN at operating voltage of 0.7 V.

Table 2
Biaxial flexural strength test results for unreduced and reduced ASC-type PENs.

Specimen no.	Flexural strength (MPa)	Remark
A-1	151.7	Unreduced
A-2	135.1	Unreduced
A-3	102.7	Reduced
A-4	117.1	Reduced

where ρ_{Ni} and ρ_{NiO} are the densities of Ni and NiO, respectively, and $\bar{m}^0_{NiO}$ is the initial weight fraction of NiO in the NiO-YSZ composite material.

According to the theory of elasticity, the relationship between the nodal displacement and the element strain can be expressed as [15]

$$\{\varepsilon\} = [B]\left\{d\right\}, \tag{26}$$

where $[B]$ is a matrix related to the nodal displacement and element strain.

The corresponding stress can be computed as follows:

$$\{\sigma\} = [D]\{\varepsilon\} = [D][B]\{d\}, \tag{27}$$

where $[D]$ is an elasticity matrix expressed in terms of the Young's modulus and the Poisson's ratio.For a given temperature gradient, the thermal strain vector is given by

$$\{\varepsilon^{th}\} = \Delta T[\,\alpha_x \quad \alpha_y \quad \alpha_z \quad 0 \quad 0 \quad 0\,]^T, \tag{28a}$$

$$\{\varepsilon\} = \{\varepsilon^e\} + \{\varepsilon^p\} + \{\varepsilon^{th}\}, \tag{28b}$$

where $\{\varepsilon\}$, $\{\varepsilon^e\}$ and $\{\varepsilon^p\}$ are the total, elastic and plastic strain vectors, respectively.

According to the principle of virtual work, a virtual change of the internal strain energy (internal work, W_σ) is offset by an identical change in the external work (W_F) attributed to the applied load. Thus, the force vector and stiffness matrix can be derived as follows:

$$\{F\} = \int [B]^T[D]\{\varepsilon\}dV, \tag{29}$$

$$[K] = \int [B]^T[D][B]dV. \tag{30}$$

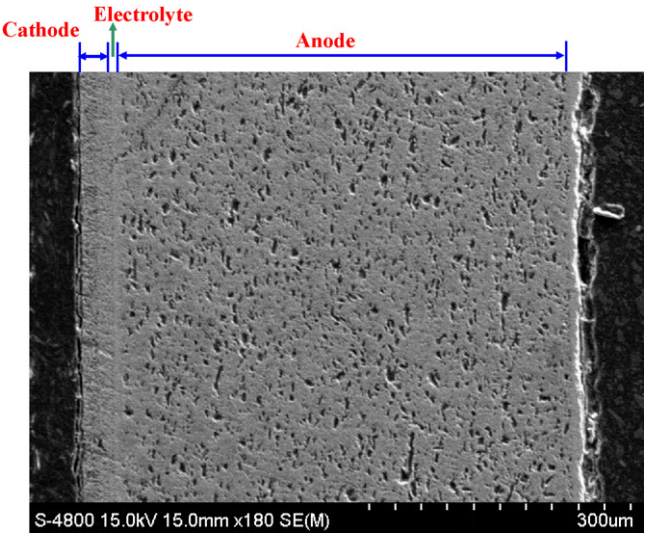

Fig. 6. SEM micrograph of fracture surface of specimen A.

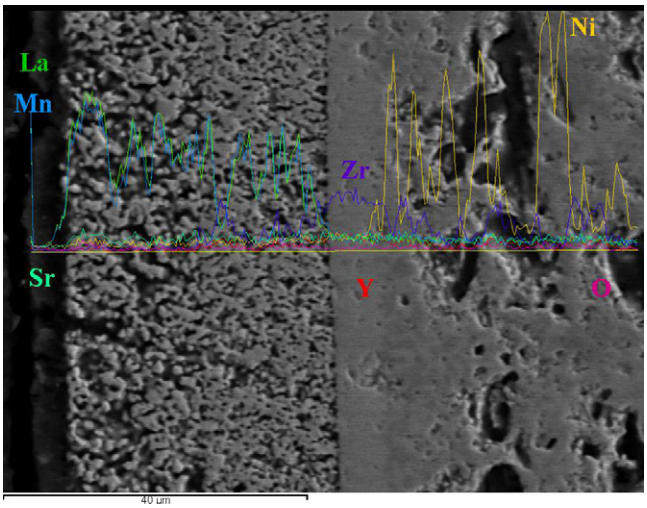

Fig. 7. EDS compositional analysis of fracture surface of specimen A.

4. Numerical and experimental results

4.1. Thermo-fluid analysis

To confirm the validity of the 3D model and the numerical solution procedure, the simulation results obtained for the variations of the cell voltage and power density with the current density were compared with the experimental results obtained from the test cell shown in Fig. 3. The corresponding results are presented in Fig. 3 for an operating temperature of 800 °C, a hydrogen flow rate of 335 ml min^{-1} and an oxygen flow rate of 670 ml min^{-1}. While the operating temperature is set at 800 °C, the real operating temperature in the center of PEN measured by thermal-couple reaches to 820 °C at V_{cell} = 0.7. From inspection, the maximum deviation of cell performance between the simulation and experimental data is found to be less than 6% and the temperature difference in the center of PEN is 5 °C at V_{cell} = 0.7. Thus, the validity of the numerical model is confirmed.

Fig. 4 illustrates the numerical results obtained for the variations of the cell voltage and power density with the current density as a function of the anode porosity. It can be seen that the power density is insensitive to the anode porosity at low values of the current density (i.e. <600 mA cm^{-2}). However, at higher current densities, the power density increases with an increasing porosity. Specifi-

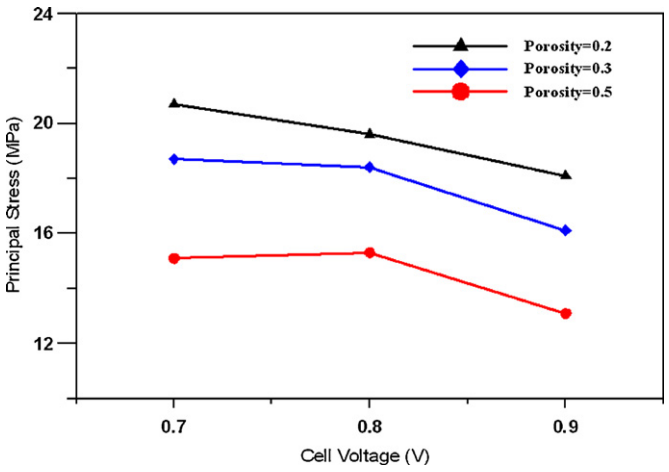

Fig. 8. Variation of maximum principal stress in PEN with cell voltage for anode porosities of 0.2, 0.3 and 0.5, respectively.

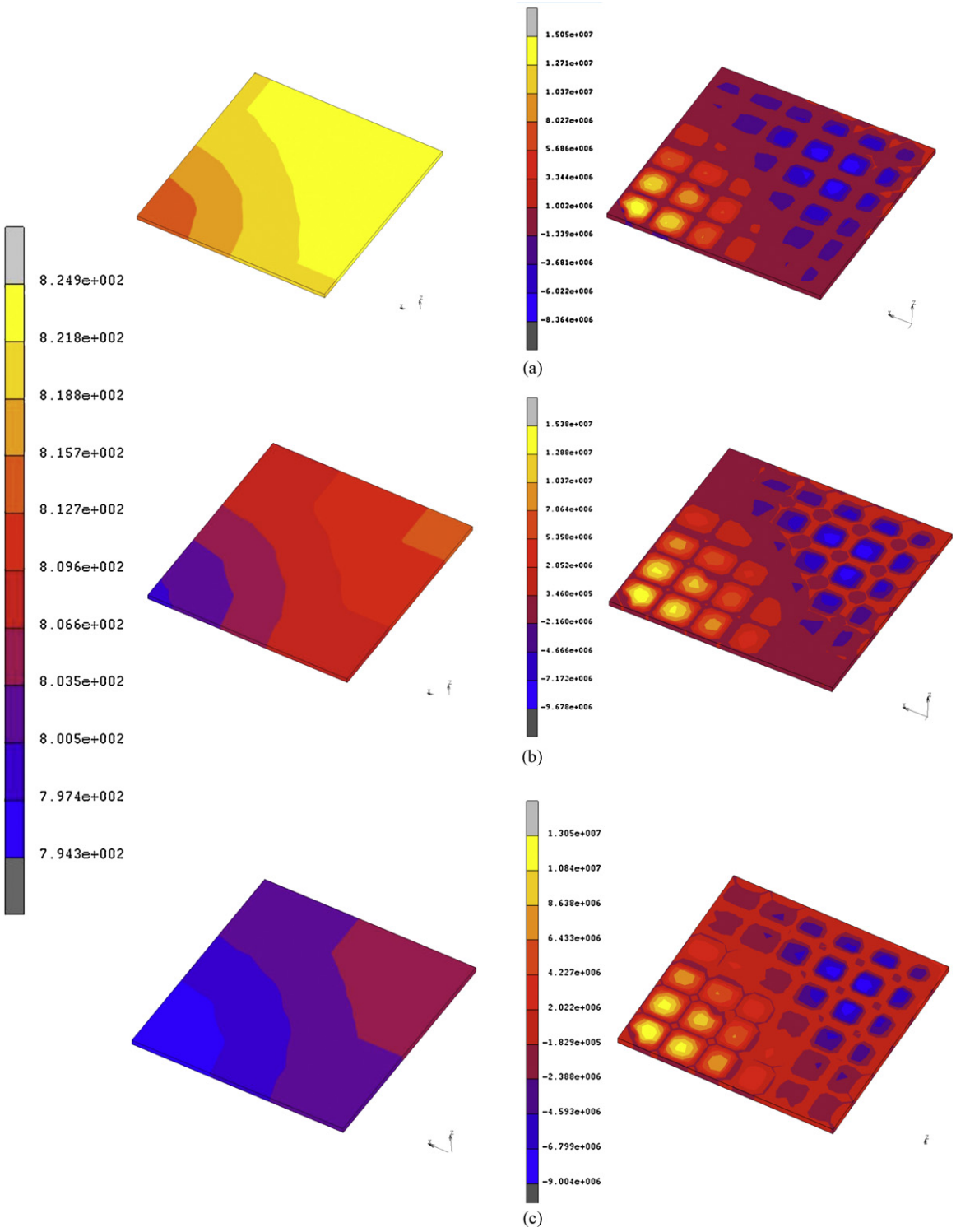

Fig. 9. Temperature gradient distributions (left) and thermal stress distributions (right) in PEN at cell voltages of: (a) 0.7 V; (b) 0.8 V; (c) 0.9 V (note that anode porosity = 0.5 in every case).

cally, the output power increases by around 10% as the porosity is increased from 0.2 to 0.3, and by a further 10% as the porosity is increased from 0.3 to 0.5. This result is to be expected since the fuel diffusion efficiency within the PEN improves as the anode porosity is increased. However, the performance improvement reduces to less than 10% as the porosity is increased beyond 0.5 due to the overpotential produced by the corresponding increase in the electronic resistance.

Fig. 5 presents the local current density distributions in the PEN for anode porosities of $\varepsilon = 0.2$, 0.3 and 0.5, respectively, and a constant cell voltage of $V_{cell} = 0.7$ V. It can be seen that in every case, the current density reduces radially from the center of the PEN toward the outlet as a result of the reduction in the concentration caused by the electrochemical reaction. Moreover, it is shown that the current density in the channel area is slightly higher than that in the rib area since the fuel diffuses directly into the electrode in the channel

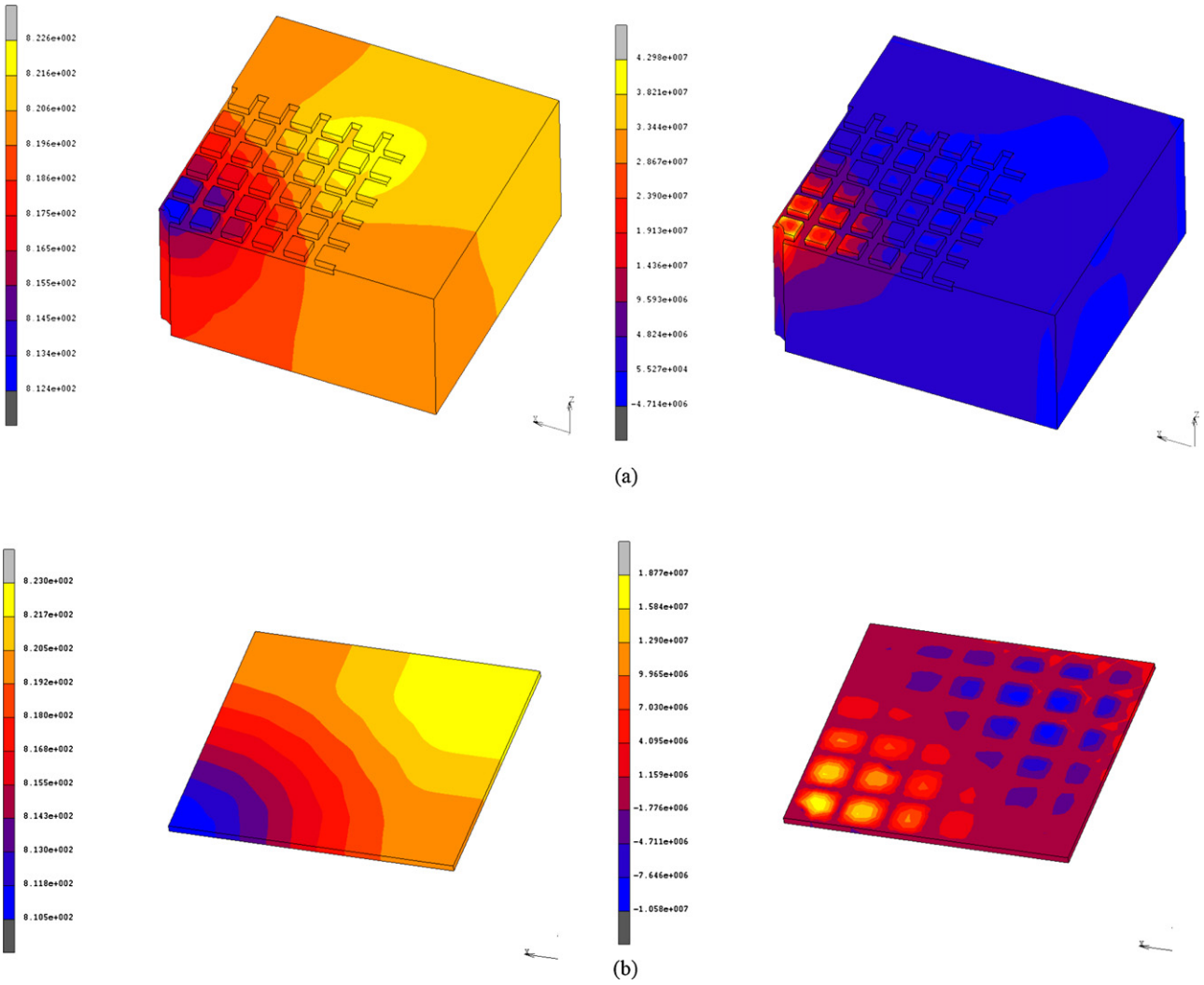

Fig. 10. Temperature gradient distributions (left) and thermal stress distributions (right) in (a) gas distributors; (b) PEN (note that cell voltage = 0.7 V and anode porosity = 0.3).

area, but travels along a longer diffusion path to reach the electrode in the rib area.

4.2. Flexural strength measurement

Ring-on-ring biaxial strength tests were performed to measure the flexural strength of four reduced and unreduced ASC PEN specimens. Table 2 presents the maximum flexural stress in each of the four specimens. It is observed that the flexural stress in specimen A (unreduced) decreases by around 25–30% in the reduced specimens. Radovic and Lara-Curzio [24] showed that the porosity of NiO-YSZ increases from 20 to 38.2% following the reduction process. In addition, it was shown that the change in porosity reduced the maximum flexural strength of the electrode from 97 MPa in the unreduced state to 68 MPa in the reduced state. In other words, the reduction process reduced the fracture strength of the Ni-YSZ anode by around 30%. This finding is in good agreement with the experimental results presented in Table 2.

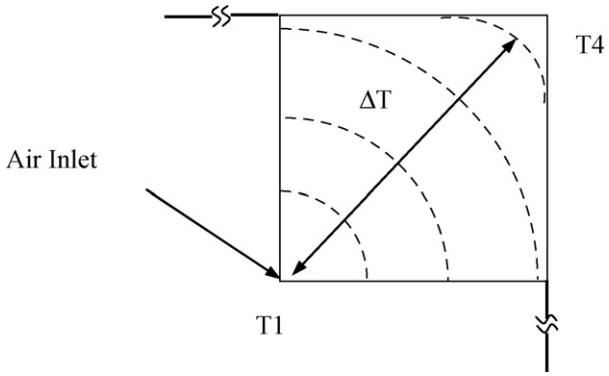

Fig. 11. Schematic definition of temperature gradient on PEN surface (one quarter model).

The fracture surfaces of the four ASC PENs were examined by scanning electron microscopy (SEM) and energy dispersive spectroscopy (EDS). Fig. 6 shows the fracture surface of specimen A (i.e. an unreduced PEN). It can be seen that the fracture surface contains a relatively uniform distribution of small cavities. These cavities are essential for gas diffusion, but should be properly controlled in order to maintain the integrity of the PEM structure. Fig. 7 presents the EDS analysis results for the fracture surface of specimen A, and shows that the dominant materials of the anode, electrolyte, and cathode are Ni, Zr and LSM, respectively.

4.3. Thermal stress analysis

Tables 3a–3c show the variations of the maximum principal stress and maximum temperature with the cell voltage (0.7–0.9 V)

Table 3a
Maximum principal stresses and temperatures at different cell voltages (porosity = 0.2).

Voltage (V)	PEN (MPa)	Gas distributors (MPa)	PEN T_{max} (°C)	PEN ΔT_{max} (°C)
0.7	20.7	42.9	821.2	12.9
0.8	19.6	40.5	809.9	12.8
0.9	18.1	37.3	808.3	12.5

Table 3b
Maximum principal stresses and temperatures at different cell voltages (porosity = 0.3).

Voltage (V)	PEN (MPa)	Gas distributors (MPa)	PEN T_{max} (°C)	PEN ΔT_{max} (°C)
0.7	18.7	42.9	823.0	12.8
0.8	18.4	42.1	811.3	12.6
0.9	16.1	36.8	806.8	11.9

Table 3c
Maximum principal stresses and temperatures at different cell voltages (porosity = 0.5).

Voltage (V)	PEN (MPa)	Gas distributors (MPa)	PEN T_{max} (°C)	PEN ΔT_{max} (°C)
0.7	15.1	42.7	824.9	12
0.8	15.3	43.5	812.7	13
0.9	13.1	36.2	805.9	11.5

for anode porosities of $\varepsilon = 0.2$, 0.3 and 0.5, respectively. Note that the gas inlet temperature is $T_i = 760\,^{\circ}C$ in every case. In theory, a lower operating voltage yields a higher current density and a higher power density, and therefore results in a higher temperature field and a greater temperature gradient (ΔT). Accordingly, Tables 3a and 3b show that the thermal stress increases with a reducing operating voltage for anode porosities of $\varepsilon = 0.2$ and $\varepsilon = 0.3$, respectively (see also Fig. 8). (Note that these results are consistent with those presented by Selimovic et al. [19].) However, as shown in Table 3c, for a higher porosity of $\varepsilon = 0.5$, the maximum thermal stress is obtained at the intermediate voltage value of 0.8 V (see also Fig. 8). This result is clarified in Fig. 9, which shows that for a porosity of $\varepsilon = 0.5$, the temperature gradient is enhanced at a voltage of 0.8 V and therefore induces a greater thermal stress within the PEN. In [24], it was shown that the reduction in the elastic modulus of the NiO-YSZ anode relative to that of the Ni-YSZ anode was directly attributable to an increased anode porosity. Hence, the reduction in the principal stress with an increasing anode porosity shown in Fig. 8 can be attributed to lower values of the elastic modulus, shear modulus and Poisson's ratio, respectively. As shown in Fig. 9(a)–(c) (right), the maximum principal stress within the PEN structure occurs at the rib edges due to CTE mismatches between the PEN and the interconnect and the effects of the contact force. Moreover, the maximum principal stress in the gas distributors is induced in the air inlet region due to the higher temperature gradient (see Fig. 10(a)).

Table 4
Maximum principal stresses in PEN and gas distributors at different temperature gradients.

Max. temperature gradients (°C) (T_1–T_4)	PEN (MPa)	Gas distributors (MPa)
50	60.1	90.7
75	91.6	137.3
100	123	184.0

Table 5
Maximum principal stresses in PEN and interconnects at different loads ($V = 0.7$, porosity = 0.3).

Load (kg cm^{-2})	PEN (MPa)	Interconnect (MPa)
0.5	18.7 (−10.5)	42.9 (−4.7)
1	18.7 (−11.1)	42.9 (−5.0)
5	18.1 (−15.2)	42.3 (−7.5)

Fig. 11 presents a schematic illustration of the temperature gradient induced within the PEN. Table 4 indicates the maximum principal stresses in the PEN and gas distributors for temperature gradients (T_1–T_4, see Fig. 11) of 50, 75 and 100 °C (7.07, 10.6 and 14.1 °C mm^{-1}), respectively. Note that T_4 is assumed to be 700 °C in every case. The results clearly show that the maximum principal stress increases with an increasing temperature gradient. According to the biaxial test results presented in Table 2, the average strength of an unreduced anode-supported PEN is approximately 135–151 MPa, depending on its composition. However, the average strength reduces to approximately 102–117 MPa after the reduction process. Table 4 shows that the maximum principal stress induced in the PEN by a temperature gradient of 75 °C (10.6 °C mm^{-1}) is 91.6 MPa. This value is close to the minimum fracture strength of the PEN (i.e. 102 MPa, see Table 2). Thus, in designing and operating the SOFC cell, the temperature gradient on the PEN surface should be carefully controlled such that it does not exceed 75 °C (10.6 °C mm^{-1}) in order to ensure the mechanical integrity of the device.

Table 5indicates the maximum principal stress within the PEN and the gas distributors for uniform loads of 0.5, 1.0, and 5.0 kg cm^{-2}, respectively. As expected, the results show that the application of a uniform load to the upper interconnect induces a compressive stress within both the PEN and the gas distributors. However, it can be seen that the magnitude of the compressive stress increases only slightly with an increasing load. Thus, it is inferred that the stress induced within the SOFC cell is the result primarily of the temperature gradient (T_1–T_4) and the effects of CTE mismatches between the various components of the cell.

5. Conclusion

This study has performed a series of numerical simulations to characterize the thermal-fluid behavior, electrochemical reactions and thermal stress properties of a planar anode-supported SOFC for various values of the operating voltage, temperature gradient and anode porosity. The validity of the numerical model has been confirmed by comparing the simulated I–V characteristics of the fuel cell with the experimental results. The numerical results support the following major conclusions:

1. For anode porosities in the range $0.2 < \varepsilon < 0.5$, the cell voltage and power density increase with increasing porosity.
2. A lower operating voltage increases the local current density and temperature gradient and therefore induces a higher principal stress within the PEN.
3. The application of a uniform load to the upper interconnect in the SOFC device induces a compressive stress within the PEN. The maximum principal stress increases only slightly with an increasing load. Thus, it is inferred that the stress within the PEN is dominated by the effects of the temperature gradient and CTE mismatches between the various components of the cell, respectively.
4. The thermal stress within the PEN is smaller at a lower temperature gradient. In practice, temperature gradient of the PEN should be less than 10.6 °C mm^{-1} in order to guarantee the structural integrity of the SOFC.

References

[1] A. Selcuk, G. Merere, A. Atkinson, J. Mater. Sci. 36 (2001) 1173–1182.
[2] H. Yakabe, Y. Baba, T. Sakurai, M. Satoh, I. Hirosawa, Y. Yoda, J. Power Sources 131 (2004) 278–284.
[3] B.F. Sorensen, S. Primdahl, J. Mater. Sci. 33 (1998) 5291–5300.
[4] F.L. Lowrie, R.D. Rawlings, J. Eur. Ceram. Soc. 20 (2000) 751–760.
[5] X. Jacques-Bedard, T.W. Napporn, R. Roberge, M. Meunier, J. Power Sources 153 (2006) 108–113.
[6] K.J. Yoon, S. Gopalan, U.B. Pal, J. Electrochem. Soc. 154 (2007) 1080–1087.
[7] W. Winkler, J. Power Sources 86 (2000) 449–454.
[8] V.A.C. Haanappel, V. Shemet, S.M. Gross, T. Koppitz, N.H. Menzler, M. Zahid, W.J. Quadakkers, J. Power Sources 150 (2005) 86–100.
[9] T.L. Cable, S.W. Sofie, J. Power Sources 174 (2007) 221–227.
[10] H. Yakabe, T. Ogiwara, M. Hishinuma, I. Yasuda, J. Power Sources 102 (2001) 144–154.
[11] H. Yakabe, T. Sakurai, J. Power Sources 174 (2004) 295–302.
[12] H. Yakabe, M. Hishinuma, M. Uratani, Y. Matsuzaki, I. Yasuda, J. Power Sources 86 (2000) 423–431.
[13] L. Andreassi, G. Rubeo, S. Ubertini, P. Lunghi, R. Bove, Int. J. Hydrogen Energy 32 (2007) 4559–4574.
[14] H. Liu, C. Lee, Y. Shiu, R. Lee, W. Yan, J. Power Sources 167 (2007) 406–412.
[15] L.K. Chiang, H.C. Liu, Y.H. Shiu, C.H. Lee, R.Y. Lee, Renew. Energy 33 (2008) 2580–2588.
[16] C.K. Lin, T.T. Chen, Y.P. Chyou, L.K. Chiang, J. Power Sources 164 (2007) 238–251.
[17] M.A. Khaleel, Z. Lin, P. Singh, W. Surdoval, D. Collin, J. Power Sources 130 (2004) 136–148.
[18] K. Johnson, M.A. Khaleel, SECA 6th Annual Workshop, April 18–21, 2005.
[19] A. Selimovic, M. Kemm, T. Torisson, M. Assadi, J. Power Sources 145 (2005) 463–469.
[20] K.S. Weil, B.J. Koeppel, J. Power Sources 180 (2008) 343–353.
[21] K.S. Weil, B.J. Koeppel, Int. J. Hydrogen Energy 33 (2008) 3976–3990.
[22] W.G. Sawyer, K.D. Freudenberg, P. Bhimaraj, L.S. Schadler, Wear 254 (2003) 573–580.
[23] K.S. Weil, J.E. Deibler, J.S. Hardy, D.S. Kim, G.G. Xia, L.A. Chick, C.A. Coyle, J. Mater. Eng. Perform. 13 (3) (2004) 316–326.
[24] M. Radovic, E. Lara-Curzio, Acta Mater. 52 (2004) 5747–5756.
[25] A. Selcuk, A. Atkinson, J. Eur. Ceram. Soc. 17 (1997) 1523–1532.
[26] A. Atkinson, A. Selcuk, Proceedings of the 5th International Symposium on SOFC. PV 97–18, 1997, pp. 671–680.
[27] R.W. Schmitt, K. Blank, G. Schonbrunn, Sprechsaal 116 (1983) 397–405 (in German).
[28] Y. Lin, S. Beale, 3rd International Conference on CFD in the Minerals and Process Industries, CSIRO, Melbourne, Australia, December 10–12, 2003.